The Astrophysical Journal, 916:68 (10pp), 2021 August 1 https://doi.org/10.3847/1538-4357/ac0150

Accretion Flow Properties of GRS 1915+105 During Its θ Class Using AstroSat Data

Anuvab Banerjee[1], Ayan Bhattacharjee[1,2], Debjit Chatterjee[3,4], Dipak Debnath[3], Sandip Kumar Chakrabarti[3], Tilak Katoch[5], and H. M. Antia[5]

[1] S.N. Bose National Centre for Basic Sciences, Block JD, Sector 3, Salt Lake, Kolkata 700106, India; ayan12@bose.res.in
[2] Ulsan National Institute of Science and Technology, Ulsan 44919, Republic of Korea
[3] Indian Center for Space Physics, 43 Chalantika, Garia St. Road, Kolkata 700084, India
[4] Indian Institute of Astrophysics, Koramangala, Bangalore 560034, India
[5] Tata Institute of Fundamental Research, Homi Bhaba Road, Mumbai 400005, India
Received 2020 July 5; revised 2021 May 4; accepted 2021 May 5; published 2021 July 28

Abstract

The Galactic microquasar GRS 1915+105 shows rich variability that is categorized into different classes. In this paper, we report the temporal and spectral analysis of GRS 1915+105 to study the properties of the accretion flow when the light curve shows θ class variability. For this purpose, we use the Large Area X-ray Proportional Counter data from the Target of Opportunity observations of India's first multiwavelength astronomy satellite AstroSat. The θ class is marked by the recurrent appearance of U-shaped regions in the light curve, where the photon count rate first decreases rapidly and then increases slowly. For our analysis, we use U-shaped regions of the first two orbits (02345 and 02346) on 2016 March 4. In both cases, the dynamic power-density spectra (PDS) showed significant power at around 4–5 Hz, suggesting the presence of a low-frequency quasi-periodic oscillation (QPO) around that frequency interval. The QPO frequency is found to increase with time when the energy flux is also enhanced. From the evolution of the spectra, we determine the evolution of the accretion flow parameters in these two observations. Fitting the spectra with the transonic flow solution-based two-component advective flow (TCAF) model in the 4–25 keV energy band shows that the Keplerian disk accretion rate increases with the increase in radiation intensity, while the location of the centrifugal pressure-driven shock front decreases. In both these data, a gradual increment of power-law photon index with intensity is observed, suggesting the progressive softening of the source.

Unified Astronomy Thesaurus concepts: X-ray binary stars (1811); Black holes (162); Accretion (14); Jets (870)

1. Introduction

Since the first discovery by the WATCH detector in 1993 (Castro-Tirado et al. 1992), the Galactic microquasar GRS 1915+105 aroused a great deal of interest in the scientific community because of its rich and enigmatic spectral and timing variability features. Especially in X-rays, the variation in luminosity by a few orders of magnitude within a span of a few tens of seconds makes it an object of great scientific interest for undertaking a spectral and temporal study in X-ray band. Soon after the discovery, the entire variability of the source was categorized into 14 different variability classes on the basis of the variability pattern, a conventional color–color diagram, and the hardness ratio (Belloni et al. 2000; Klein-Wolt et al. 2002). The observed recurrence of these classes was a unique feature of this source.

Phenomenologically, the X-ray spectra of most X-ray binaries can be explained using a thermal and a nonthermal component. The thermal component is contributed by the Keplerian accretion disk, emitting at different temperatures from successive concentric shells (Shakura & Sunyaev 1973). The nonthermal part is generated by the inverse Comptonization of soft-disk photons in the coronal region around the black hole (Sunyaev & Titarchuk 1980; McClintock & Remillard 2006), which may be called a Compton cloud. The spectral and temporal study of transient, variable, and persistent sources is necessary to obtain a comprehensive picture of the accretion processes around such objects. It was suggested by Belloni et al. (2000) that in the case of GRS 1915+105, the transition between all the different variability classes may be due to the transition between three basic states A, B, and C. States A and B are characterized by spectral softness, the only difference is that the inner disk temperature of B is comparatively higher than that of A. In the case of C, the spectrum is dominated by a hard power-law component, and the inner disk region is practically nonexistent. The description of the spectral and temporal behavior of GRS 1915+105 as a transition between these three fundamental classes is a unique feature of this object itself and is markedly different from the standard transient source behaviors (Tanaka & Lewin 1995). Qualitative physical pictures of these states and other possible states of the variability class transitions were presented immediately (Chakrabarti & Nandi 2000; Nandi et al. 2000).

State C or the harder state is marked by the occurrence of 1–15 Hz quasi-periodic objects (QPOs). Investigating the origin of 1–15 Hz QPO of GRS 1915+105, Markwardt et al. (1999) reported that QPOs are predominantly present during spectrally hard dips in the flaring states and that the oscillation frequency is strongly correlated with the thermal flux. As the power-law flux is reduced and the spectral slope steepens toward the end of the dips, the QPO disappears, suggesting the presence of two spectral components that interact. Chakrabarti & Manickam (2000) showed that the QPO frequency can be explained by the radial oscillation of the post-shock region, and the transition from soft X-ray domain (burst-on states) to hard dips (burst-off states) and that the mean time of residence in these states could be explained by outflows from the post-shock region. They further observed that QPOs are suppressed for thermal photons (0–4 keV), but become prominent for nonthermal photons (4–13 keV), clearly indicating that the QPO phenomenon arises from Comptonized photons

(Rao et al. 2000). Investigation of the energy dependence of low-frequency QPOs of GRS 1915+105 using RXTE data further establishes the inverse Comptonization of the soft-seed photons by the "corona" participating in the QPO activity, and its frequency variation is strongly correlated with soft X-ray flux (2–5 keV; Rodriguez et al. 2002). However, it was observed during the analysis of α and β classes of GRS 1915 +105 that the QPO frequency changes during the passage of hard dips, where the soft X-ray flux remains roughly unchanged (Mikles et al. 2006). This further demonstrates the broad correlation of QPO frequency and power-law flux indicated by Markwardt et al. (1999) as well, which gradually weakens toward the latter half of the dip. It had, however, been argued that the two spectral components cannot really be disentangled. This was further supported by the spectro-temporal analysis of GRS 1915+105 by Rodriguez et al. (2008), who studied the energy dependence of low-frequency QPOs (LFQPO) in the hard-intermediate state. The importance of both components has also been highlighted during an energy-resolved LFQPO analysis to pinpoint the origin of QPOs (Rao et al. 2000; Vadawale et al. 2001).

Several attempts were made by different groups to determine the origin of QPOs in general. The proposed mechanisms include relativistic precessions of encircling matter due to misalignment of the black hole spin axis and inner accretion flow region (Ingram et al. 2009) as well as instability in the inner disk region (Tagger & Pellat 1999). Fitting the phase-resolved spectra using Comptonization, edge smearing, and a Gaussian equivalent width model, Ingram & van der Klis (2015) suggested the geometric origin of the QPOs.

In the two-component advective flow (TCAF) model, the angular momentum of the inflow is redistributed to form two components: (i) the higher-viscosity Keplerian disk on the equatorial plane surrounded by (ii) the lower viscous and lower angular momentum flow (Chakrabarti 1995; Chakrabarti & Titarchuk 1995 hereafter CT95; Chakrabarti 1996). It was shown by Chakrabarti and his collaborators that the resonance oscillation of the shocked surface can produce the observed low-frequency QPOs (Molteni et al. 1996; Chakrabarti et al. 2015). Soft-seed photons from the Keplerian disk intercepted by the shock are inverse-Comptonized by hot electrons in the post-shock region, technically known as the centrifugal pressure supported boundary layer (CENBOL; Chakrabarti 1996, 1997; for the nature of different spectra and additional references, see CT95). More recently, the stability of the TCAF solution was established (Giri & Chakrabarti 2013) and the Monte Carlo simulation-generated QPOs and observed ones were demonstrated to be similar (Garain et al. 2014). If the cooling timescale in the CENBOL roughly matches the infall (i.e., compressional heating) timescale from the shock front, resonance oscillation of the shock surface is triggered. The oscillation frequency depends on the shock distance from the black hole and the shock strength (Chakrabarti & Manickam 2000), which in turn is determined by the viscosity in the equatorial plane. The viscosity enhancement prompts the conversion from the sub-Keplerian into the Keplerian flow, which enhances soft photons cooling the CENBOL. Because the QPO frequency is inversely proportional to the infall timescale, the frequency increases with the increase in Keplerian disk rate, which controls the cooling (Mondal et al. 2015). During the rising phase of an outburst, the shock gradually moves toward the black hole, and the QPO frequency steadily increases. Exactly the opposite trend is observed in case of the declining phases, especially in the hard state (HS) and in the hard- intermediate state (HIMS; Debnath et al. 2013). To directly fit black hole energy spectra with the spectrum from the TCAF model and extract physical flow parameters, this model has been implemented in 2014 as a local additive table model in XSPEC (Debnath et al. 2014, 2015a). After this, many transient, persistent sources were studied with this model to understand the accretion dynamics of these objects (Debnath et al. 2014, 2015a, 2015b, 2017, 2020; Mondal et al. 2014, 2016; Chatterjee et al. 2016, 2019, 2020a, 2020b; Jana et al. 2016, 2020a, 2020b; Bhattacharjee et al. 2017; Shang et al. 2019; Banerjee et al. 2021). The masses of unknown black hole candidates were also estimated with better accuracies based on the constant model normalization method described by Molla et al. (2016). Estimates of X-ray fluxes of the jet and its properties were studied for a few short orbital periods in case of black hole X-ray binaries using the method described by Jana et al. (2017). The TCAF solution was successfully applied to study the spectral and timing properties of accretion around neutron stars (Bhattacharjee & Chakrabarti 2017; Bhattacharjee 2018; Bhattacharjee & Chakrabarti 2019, 2020, 2021).

Satellites with broadband instruments play an important role in providing an opportunity to perform both the spectral and the temporal analysis over a wide band of wavelengths to derive a complete scientific understanding of these accretion flow mechanisms around accreting objects. The Indian satellite AstroSat offers such a platform for simultaneous observation in 0.3–100 keV with its coaligned instruments, the Large Area X-ray Proportional Counter (LAXPC; Yadav et al. 2016a, 2016b; Antia et al. 2017), the Soft X-ray Telescope (Singh et al. 2017), and the Cadmium Zinc Telluride Imager (Vadawale et al. 2015). Banerjee et al. (2020) carried out spectral analyses of GRS 1915 +105 in its χ class to determine the physical properties of its radio-loud and radio-quiet subclasses. In the present paper, we study another important variable class of the source, namely θ in the TCAF paradigm.

We report the spectral and timing analysis of the θ class data from a small subset of a AstroSat target of opportunity (ToO) observation on 2016 March 4 by the onboard LAXPC instrument. We investigate the evolution of the spectral and temporal behavior and the QPOs (if any), and derive the underlying accretion flow parameters causing the observed evolution. The organization of the paper is as follows: in the next section, we present the details of our observation and data reduction techniques. The detailed results of the timing and spectral analysis are provided in Section 4. Finally, in Section 5, we draw the final conclusions.

2. Observation and Reduction of Scientific Data

The capability of a detailed spectro-temporal study of LAXPC has already been demonstrated for several X-ray binaries (Yadav et al. 2016a; Misra et al. 2017; Pahari et al. 2017, 2018). The LAXPC instrument consists of three identical but independent X-ray proportional counters that can register photons in 3–80 keV with a time resolution of 10μs (Yadav et al. 2016a, 2016b; Agrawal et al. 2017). We have carried out our analysis on the basis of instructions provided in the LAXPC analysis software `LaxpcSoft` released on 2019 May 16.[6] The details of the data analysis procedure using background and response matrices are provided by Antia et al. (2017).

[6] https://www.tifr.res.in/~astrosat_laxpc/archived.html

Table 1
The Variation of QPO Frequencies, Respective Q-values, and rms Powers are Shown with Respect to Time

Orbit No.	Time Segment (S)	QPO Frequency (Hz)	Q Value	rms (%)
	50-150	4.22 ± 0.05	10.0 ± 0.2	7.3 ± 0.2
02345	75-175	4.27 ± 0.05	12.7 ± 0.2	6.7 ± 0.3
	100-200	4.41 ± 0.04	7.6 ± 0.1	7.3 ± 0.2
	125-225	4.51 ± 0.09	11.3 ± 0.1	5.6 ± 0.3
	332-348	5.39 ± 0.04	6.0 ± 0.1	6.5 ± 0.3
	348-364	4.87 ± 0.03	3.8 ± 0.1	8.9 ± 0.3
	364-380	4.20 ± 0.04	7.9 ± 0.1	11.5 ± 0.3
	380-396	3.69 ± 0.05	3.7 ± 0.2	11.9 ± 0.2
	400-500	2.90 ± 0.05	7.8 ± 0.2	9.4 ± 0.3
	425-525	2.98 ± 0.03	8.3 ± 0.1	11.4 ± 0.3
	450-550	3.02 ± 0.05	6.7 ± 0.2	11.0 ± 0.3
	475-575	3.11 ± 0.03	8.7 ± 0.1	9.5 ± 0.3
	500-600	3.25 ± 0.04	5.7 ± 0.2	10.8 ± 0.2
02346	525-625	3.38 ± 0.04	6.0 ± 0.1	9.4 ± 0.2
	550-650	3.56 ± 0.05	5.9 ± 0.1	9.2 ± 0.2
	575-675	3.77 ± 0.06	5.7 ± 0.1	9.2 ± 0.2
	600-700	3.81 ± 0.06	6.2 ± 0.1	10.1 ± 0.3
	625-725	3.92 ± 0.05	6.2 ± 0.1	9.4 ± 0.2
	650-750	4.05 ± 0.07	8.6 ± 0.2	7.7 ± 0.2
	675-775	4.28 ± 0.09	8.1 ± 0.1	5.8 ± 0.3
	700-800	4.33 ± 0.06	5.2 ± 0.1	6.3 ± 0.3

Note. All the time stamps are relative to t_0 of the corresponding orbit. Here, 2016 March 4 data of AstroSat orbit number 02345 and 02346 are used. t_0 for 02345 is defined at UT 12:01:26, i.e., at MJD = 57451.501. For the following orbit, t_0 is defined at UT 13:42:14, i.e., at MJD = 57451.571. The QPO frequency slowly drifts as time evolves.

Notwithstanding the wealth of data of RXTE on GRS that are available for general usage, there are certain advantages in using AstroSat data. The effective area of RXTE PCA quickly decreases with increasing energies. Around 30 keV, the effective area of LAXPC ($\sim$4500 cm^2) is significantly higher than that of RXTE PCA ($\sim$1000 cm^2; Yadav et al. 2016b, Table 1). Furthermore, the time resolution of the standard two-mode data in RXTE (used for spectral analysis) is 16 s, while LAXPC gathers event-mode data at high time resolution (10μ s), which is very useful in the analysis of highly variable sources. For the purpose of our analysis, ToO level 1 data were obtained from the ISSDC data distribution archive.[7] Only the data from LAXPC10 of the three LAXPC detectors were used in our analysis. For the spectral analysis, the source and background spectra have been generated. The corrections for the South Atlantic Anomaly, Earth occultation, and dead time were made with the LAXPC software. In order to avoid the undesirable contribution from an instrumental artifact, namely, a bump at $\sim$33 keV (Antia et al. 2017), only the 4.0–25.0 keV energy range is considered. Data from all the anodes in the detector have been used for analysis. For the spectral analysis, `XSPEC v 12.9.1` was used.

In the entire $\sim$67 ks of the LAXPC10 exposure, the data were recorded during a span of nine satellite orbits (02345–02354) starting from 2016 March 4 11:22:15 to 2016 March 5 04:54:23. All the light curves in θ class (Belloni et al. 2000) repeatedly exhibit an M shape with a duration of a few hundred seconds, with brief intervals with a low count rate. We have selected U-shaped regions in the M-shaped θ class data of the initial two AstroSat orbits, i.e., 02345 and 02346 (Figures 1(a) and (b)). In orbit 02345, this phase spans over 460 s (Figure 1(a)), and in the following orbit, this steady rising phase spans over a wider time period of $\sim$800 s (Figure 1(b)). The start times of observation in the first and the following orbits correspond to UT 12:01:26 and UT 13:42:14 on 2016 March 4 (MJD = 57451.501 and 57451.571, respectively). In our analysis, we treat these times as $t_0 = 0$.

For the first orbit, the photon flux in the entire interval varied from $\sim$2700 count s^{-1} to $\sim$7000 count s^{-1} (Figure 1(a)). In the case of the second orbit, the same flux varies from $\sim$2000 count s^{-1} to $\sim$9000 count s^{-1} (Figure 1(b)). In order to search for any continuous variation of the timing behavior, we adopted a dynamic method for the timing analysis. The individual power-density spectrum (PDS) in the 4–25 keV for the time span of one hundred seconds is generated using the standard HEASoft XRONOS package task "powspec" with a suitable normalization (equal to -2) to eliminate the white-noise level. For the purpose of analysis, we extracted light curves of 0.01 s time resolution, which corresponds to the Nyquist frequency of 50 Hz. Each light curve was divided into 4096 time bin intervals, and then the PDS was created for each interval. The final PDS was obtained by averaging over all these individual PDS. The average PDS was binned with a bin size that increased by a factor of 1.03 in frequency space. In the generation of dynamic PDS, each successive PDS is shifted by 1 s from the previous one. The PDSs are plotted in a 3D color map with a suitable color palette.

In the dynamic PDS, a significant concentration of power is observed within a narrow frequency band for a certain observation span. Individual PDSs were extracted with suitable time resolution and time bin intervals in order to search for the plausible peaked component on top of the broadband noise. The details are provided in Section 3.2. The PDS were fit using Lorentzian and power-law components in order to take care of the QPO and the broadband component of the noise, respectively. Specific attributes corresponding to the peaked component, viz. the centroid frequency, Q factor, and contributed rms power, were determined from the fit parameters. The error values were determined using the built-in "fit err" method.

Within the region of interest in both orbits, the photon count increased significantly. Therefore the spectra covering the entire energy domain were not analyzed as a whole. Instead, the entire domain was split into subdomains depending on the intensity variation. In the case of the first orbit, the analysis domain was split into five subdomains: the first is the 60 s interval containing the declining phase, and the other four are 100 s intervals in the subsequent rising phase of 400 s. In the case of the second orbit, the rising phase of $\sim$700 s was split into equal subintervals of 100 s each. Spectral analysis was carried out to obtain the parameter evolution, and in light of this, to understand the timing result. During the entire observation span, the hydrogen column density (N_H) was kept fixed at 6.0×10^{22} cm^{-2} (Muno et al. 1999) and was modeled using the absorption model *phabs*. In order to obtain a quantitative measure of the shift in spectral hardness, each background-subtracted spectrum was fit using the *phabs*(diskbb +power-law)* model. Subsequently, in order to have a physical picture of the accretion flow, we analyzed the same spectra using phabs*TCAF as well. For this purpose, the TCAF-based model *fits*

[7] https://astrobrowse.issdc.gov.in/astro_archive/archive/Home.jsp

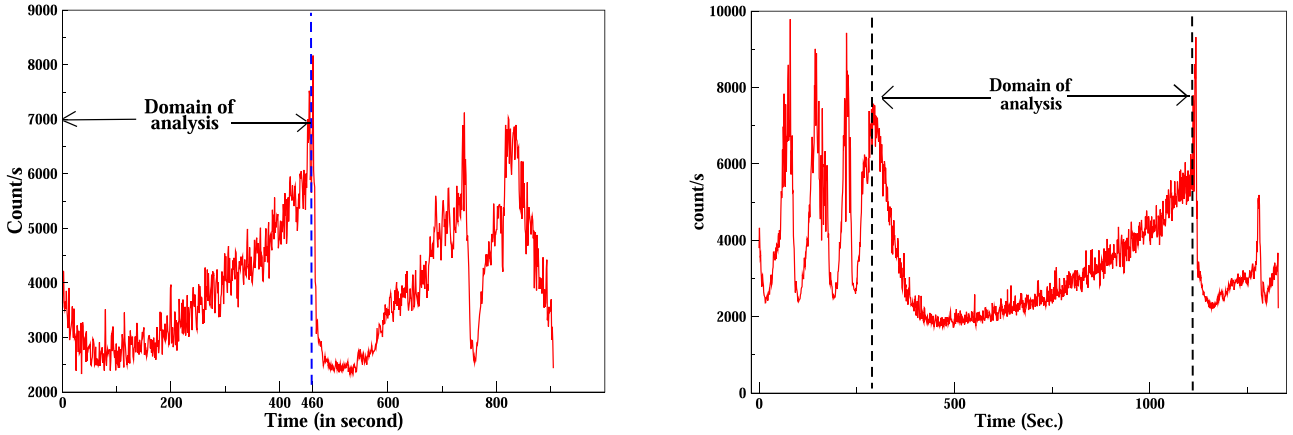

Figure 1. (a) In the left panel, the domain of analysis corresponding to orbit 02345 is indicated. For the purpose of our spectral and timing analysis, we took the first 460 s of data, namely the U-shaped curve of θ class. In the first ∼60 s, the photon count is declining, after which it increases monotonically. All the time stamps are relative to t_0 (MJD = 57451.501). (b) In the right panel, the domain of analysis corresponding to orbit 02346 is indicated. The time stamps are relative to $t_0 = 57451.571$.

file was used (TCAF_v0.3.2_R1.fits). Four flow parameters (a–d) and one system parameter (e) were used to achieve the best fit: (a) the Keplerian disk accretion rate, $\dot{m}_d$ (in units of $\dot{M}_{\rm Edd}$), (b) the sub-Keplerian halo accretion rate, $\dot{m}_h$ (in units of $\dot{M}_{\rm Edd}$), (c) the location of the shock front X_s (in units of Schwarzschild radius $r_g = 2GMc^{-2}$), (d) the compression ratio of the shock R, and (e) the mass of the black hole (in units of solar mass $M_\odot$). In order to obtain the best fit, we used a broad Gaussian profile as well to take care of iron line emission. A 2% systematic error was applied to achieve the best fit (see Pahari et al. 2017), and the XSPEC command "err" was used to obtain 90% confidence error values for the spectral model fit parameters.

3. Results

3.1. Nature of the Light Curve

The light curves in orbits 02345 and 02346 are shown in Figures 1(a) and (b), respectively, where the domains of our timing analysis are clearly marked. In the case of the first orbit, the left side of the vertical line indicates the domain within which we performed the timing analysis. For ∼60 s after the beginning of the observation, the photon count rate decreases. Subsequently, for ∼100 s, the count rate remains almost steady, and then it monotonically increases for ∼300 s. In the following orbit, we chose only the declining and subsequent rising phase from the middle segment of the observation. Within a span of ∼700 s, the photon count rate varied between ∼2000 and ∼7000 count s^{-1}.

3.2. Timing Analysis

For the timing analysis, we have generated the dynamic PDS for different observation domains in both orbits. The dynamic PDS has been generated by staggering individual PDSs of 100 s each, such that the origin of each successive time-series advances by one second. In Figure 2(a) we show the dynamic PDS for the first 460 s of observation in orbit 02345 to investigate the presence of some frequency domain where the power is concentrated. The x-labels stand for the midpoint of the respective time windows chosen for the generation of the dynamic PDS. We observe two oscillation modes that contribute significantly to the overall power. The strongest oscillation mode is observed at around 4–5 Hz, which is the focus of our paper, although there is another low-powered and lower-frequency oscillation mode at ∼2 Hz in the first ∼250 s as well. With the passage of time, we observe a slight drift in this domain of concentrated power. The dynamic PDS generated using the same procedure from the data marked in Figure 1(b) is shown in Figure 2(b). The upward trend in the power-concentrated domain is apparent here as well.

In order to observe the behavior of the peaked components in the PDS during the sharp declining phases of the two orbits more closely, we generated the dynamic PDS corresponding to this domain separately. The only 60 s duration of the declining phase in case of orbit 02345 and the sharp decline within ∼100 s in case of the the following orbit implies that the PDS has to be produced for smaller time windows to obtain a reasonable PDS that is representative of the declining phase alone and is not contaminated by the contribution from the rising phase at all. With 100 s of data blocks, we pick up noise and peaked components both from the declining and the rising phases. However, for smaller data blocks, the corresponding time series needs to be divided into more "newbin intervals" during the production of individual PDS using "powspec" to ensure the pruning of unwanted noise components. Considering these issues, the data corresponding to this declining phase were extracted keeping the time resolution of 0.001 s for the purpose of generating a dynamic PDS. Each individual data block was considered to be of 16 s, and the origin of each successive data segment was advanced by 1 s. Figure 3(a) and (b) features the dynamic PDS for the declining arm corresponding to the two orbits 02345 and 02346, respectively. For 02345, the power is concentrated between 4–5 Hz for the entire phase. In the case of 02346, however, we observe a conspicuous downward trend in the peaked component in frequency space.

We investigated individual PDSs to search for the presence of a strong peaked component over the broadband noise. In the case of orbit 02345, a closer look at the individual PDSs yields the presence of such peaked components in the first 225 s of observation, starting from the onset of the rising arm of the U-shaped curve of interest. In the case of the following orbit, the peaked component is observed in the first 400 s of observation during the monotonic increase in photon flux in the

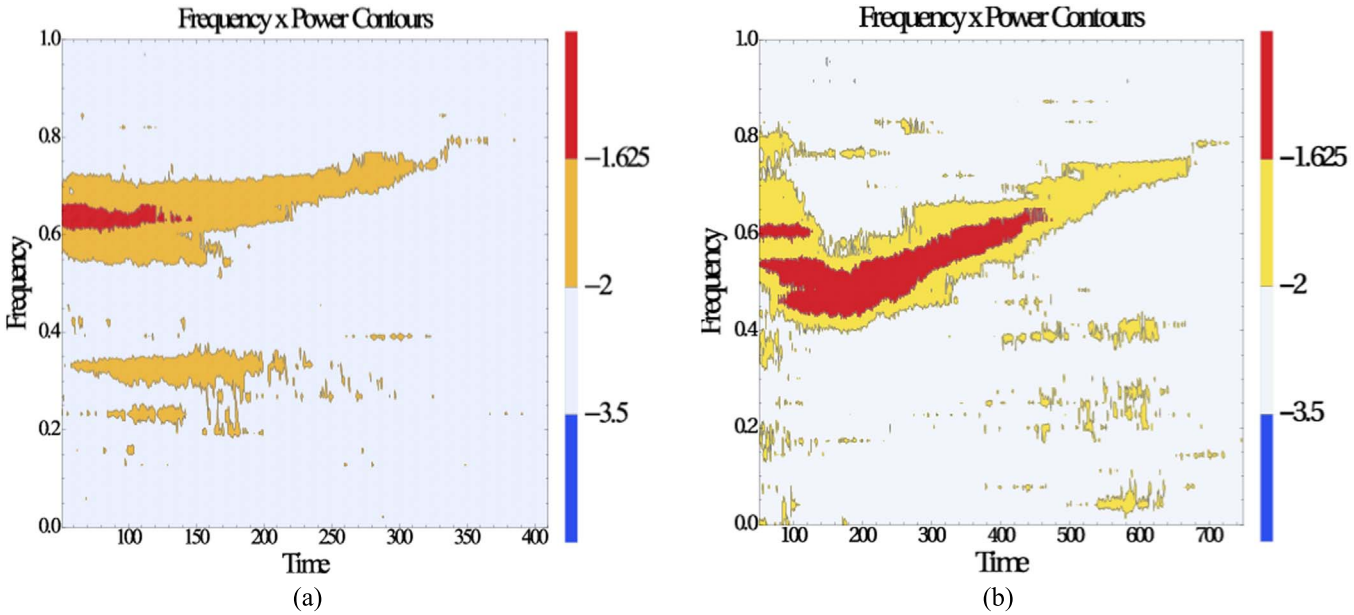

Figure 2. (a) The PDS for the first 460 s of observation orbit no. 02345 is shown. The *x*-axis is the observation time in seconds (with t_0 at MJD = 57451.501), the *y*-axis is the Fourier-transformed frequency (in Hz), and the color bars represent the logarithm of the frequency multiplied by the power. Note that *y*-axis and color bar are plotted in $\log_{10}$ units. The strongest oscillation modes have been found to be around 4 Hz, and this mode is conspicuous for about the first 225 s. This domain has been chosen for the spectral analysis. In addition, the low-frequency oscillation at ∼2 Hz is also obtained. (b) Corresponding to orbit 02346, we have shown the dynamic PDS for the entire domain of our analysis as indicated in Figure 1(b). The zeroth of the time stamps stand for 300 s after the initiation of observation for orbit 02346 (=MJD 57451.571), i.e., MJD 57451.574. The low-frequency oscillation mode is absent, and the strongest oscillation mode lies around 3–4 Hz.

rising arm. Peaked components are also detected during the initial declining phase in both orbits. The PDS are fit with the combined Lorentzian and power-law models to account for the peaked (QPO) component and broadband noise, respectively. The corresponding parameters quantifying the peaks, namely the centroid frequency, the rms power, and Q factor (=centroid frequency/full width at half maximum) are determined. In the case of the first orbit, during the declining phase, the centroid frequency was found to be around 4.3 Hz, with the rms power varying in the range 7.5%–9.2%. The Q factor was found to be more than 5 throughout. During the rising phase, the centroid frequency drifted from 4.22 to 4.51 Hz. The Q factor was observed to be varying between 7.6 and 12.7. This high Q factor indicates that these peaks can be qualified as QPOs. The rms power dropped from 7.3% to 5.6%. The details of the analysis are provided in Table 1. A typical Lorentzian model fit around the QPO frequency is shown in Figure 4 (left).

We fit the lower-frequency QPOs using Lorentzian profiles as well. The centroid frequency varied within the range 2.05–2.13 Hz, with the Q factor in the range 6.5–7.0. The rms power contribution was found to be ∼7%. In addition to the principal contribution at around 4 Hz, another oscillation mode at lower frequency is another feature of our observation.

The 4 Hz QPO does not seem to be the harmonic of 2 Hz QPO. The 4 Hz QPO is more prominent and sharper, and the normalization is higher. The dynamic PDS also suggests that the dominant concentration of power is around 4 Hz. However, detailed exploration of the characteristics and the physical origin of the subdominantly peaked components merits a full-length study by itself and is beyond the present investigation.

In the following orbit, the QPO frequency during the declining phase is reduced from 5.39 to 2.90 Hz in a span of ∼100 s. The Q value resides between 3.8 and 7.9 during this period, with the rms power varying from 6.51% to 11.87%. In the rising arm, on the other hand, the centroid frequency increases from 2.90 to 4.33 Hz in the domain of our investigation. We did not obtain any consistent trend in the Q value or rms power. The Q factor resides in the range of 5.2 to 8.7, and the rms power is observed to vary between 5.8% and 11.4%. The details of the parameters, i.e., the QPO frequency, the Q value, and the rms power, are noted in Table 1.

3.3. Spectral Analysis

The dynamic spectra for both the orbits in their entire observation span are shown in Figure 5(a) and (b). In order to produce the dynamic spectrum, we have produced an individual spectrum using a 25 s duration data block and then shifting the data block by 1 s. The constant intensity contours repeatedly showed the same pattern even within the observation in one complete orbit. Hence, in order to extract a quantitative estimate of the dynamics of the flow parameters with the evolution of time, fitting of individual spectra using empirical and physical models was performed only within the first U-shaped curve in the first orbit and the prominent U-shaped curve in the second segment of the second orbit.

For orbit 02345, for the first ∼60 s, the count rate gradually decreases and becomes steady for ∼100 s. In order to determine the flow parameters in all these different domains, the data have been split into five segments. The first segment comprises 0–60 s data where the count rate decreases. Within the interval of 160–460 s, where the photon count rate increases almost monotonically, the data have been split into three segments of 100 s each. The power-law photon index changes from 2.602 to 2.546, indicating a transition to relative hardness within this short interval. Subsequently, the photon index increases to as high as 3.014, indicating a gradual softening throughout this period. In order to obtain a quantitative estimate of this transition in terms of physical parameters such as accretion rate and shock location, we

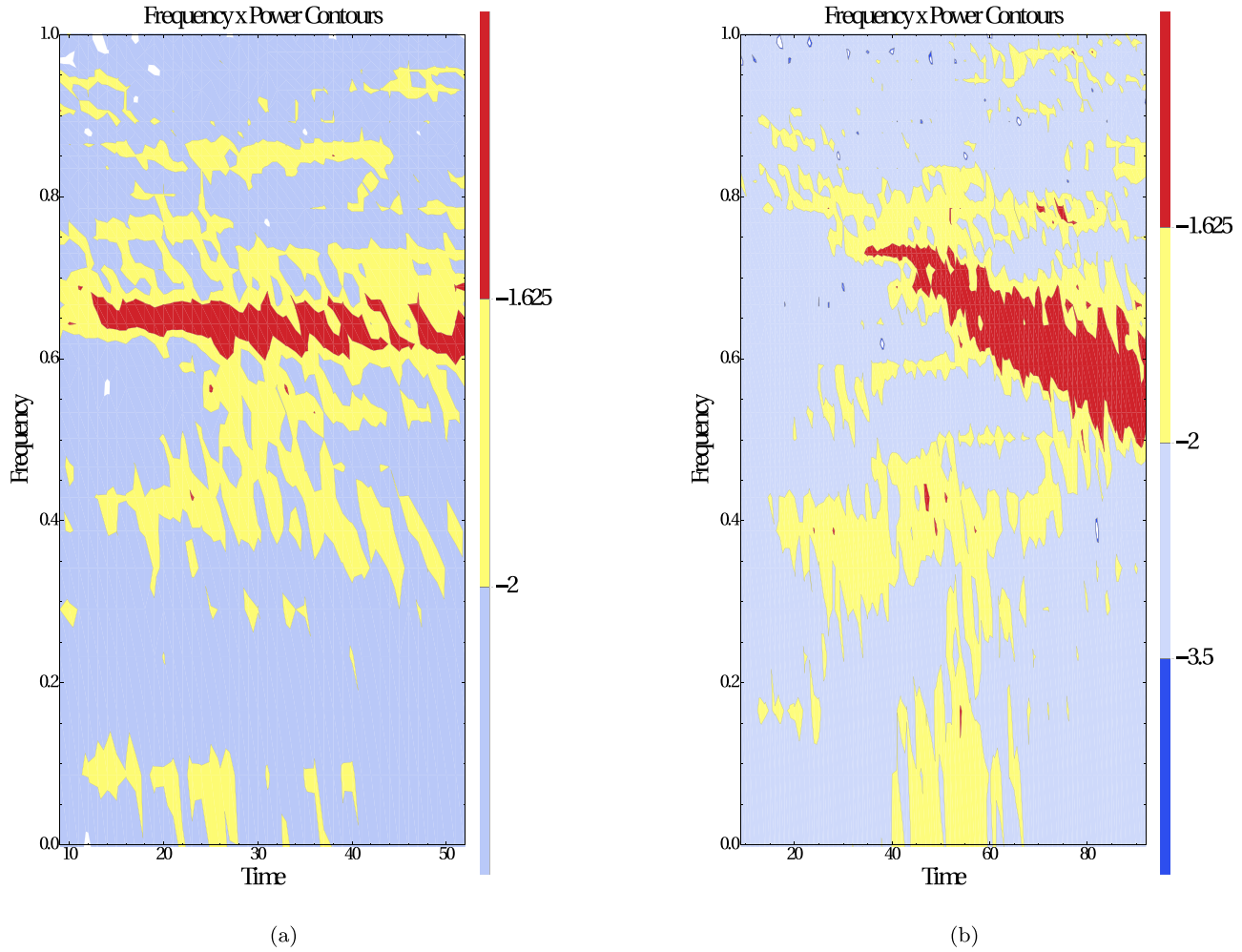

Figure 3. (a) The PDS for the first 64 s of observation corresponding to orbit 02345 is shown. The x-axis represents the observation time in seconds (with t_0 at MJD = 57451.501), and the y-axis is the Fourier-transformed frequency (in Hz). The color bar represents the frequency multiplied by the power. Both the y-axis and the color bar are provided in $\log_{10}$ units. The x-labels stand for the midpoint of the corresponding data blocks. The strongest oscillation modes have been found to be within 4–5 Hz. (b) The dynamic PDS corresponding to the fast declining phase in the domain of our analysis as indicated in Figure 1(b) is shown. The time stamps are relative to the t_0 of orbit 02346 (= MJD 57451.571), i.e., MJD 57451.574. The declining trend in the power-concentrated domain from 30 s onward is apparent.

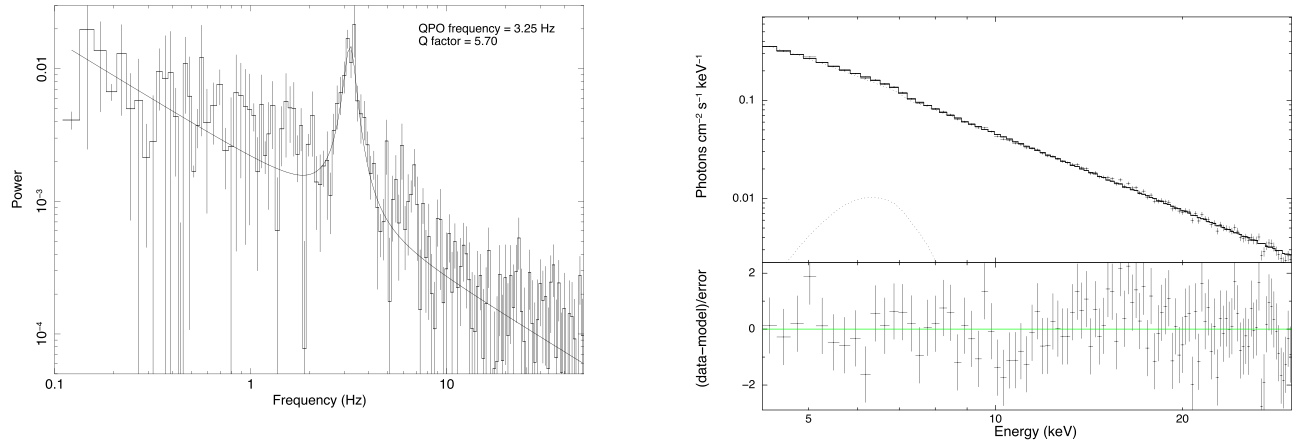

Figure 4. (Left) We show the power-density spectrum obtained for 500–600 s observation in orbit 02346. From the Lorentzian fitting, the QPO frequency turned out to be 3.25 Hz, and the Q factor was found to be 5.70. The rms power contribution was 10.79%. (Right) The 4–25 keV phabs*(TCAF+Gaussian) fitted unfolded spectrum with residue for the 0–60 s observation for orbit 02345 is shown.

further performed the spectral analysis using TCAF+Gaussian model. The variation in the flow parameters in the TCAF +Gaussian model in 4–25 keV, namely the disk rate ($\dot{m}_d$), the halo rate ($\dot{m}_h$), and the shock location (X_s), corroborate the result obtained from the empirical results. For the purpose of the spectral analysis using TCAF, the mass is kept frozen at $14.0 M_{\odot}$.

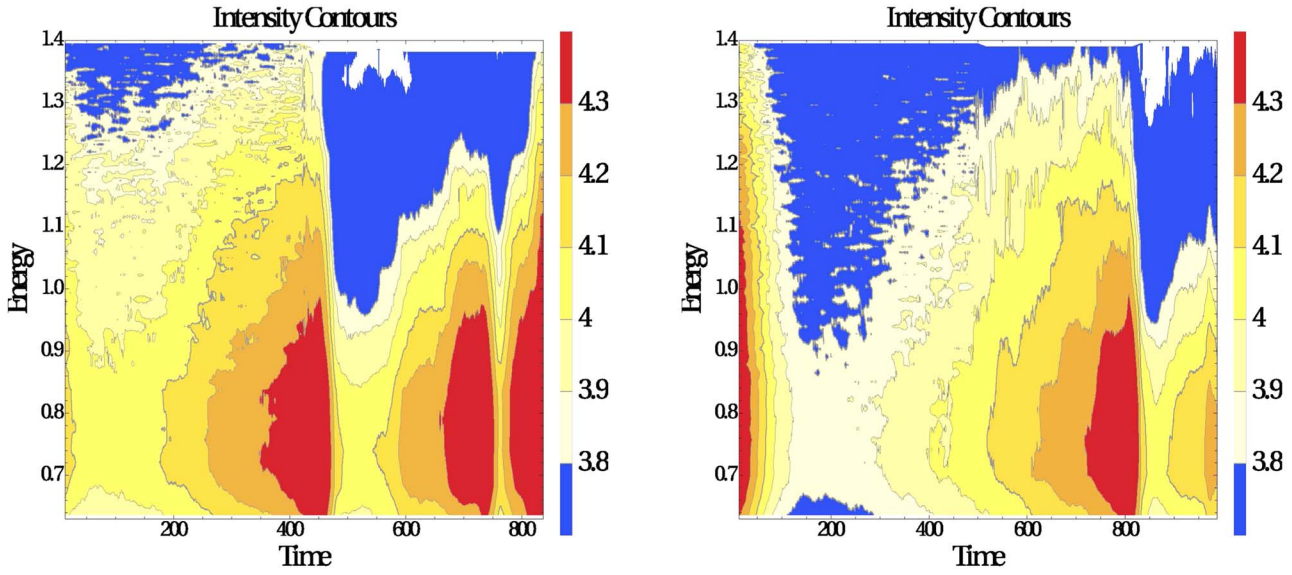

Figure 5. (a) The dynamic spectrum for the entire range of orbit 02345. The contours of the constant intensity show similar patterns in different U-shaped branches of θ class. (b) Dynamic spectra for ∼1000 s starting from the onset of the U-shaped region as indicated in Figure 1(b). Within the domain of analysis, the constant intensity contours indicate the gradual softening of the spectra.

Table 2

For the Domain of Analysis in Orbits 02345 and 02346, the Variation in TCAF Fit Parameters, Namely the Disk Accretion Rate ($\dot{M}_d$), the Halo Rate ($\dot{M}_h$), the Shock Location (X_s), the Shock Strength (R), and the Power-law Photon Index Obtained from the *diskbb + power-law* Model with Respect to Time Are Shown. The Mass of the Black Hole Is Kept Frozen

Orbit No.	Time Segment (Second)	$\dot{m}_d$ ($\dot{M}_{\rm Edd}$)	$\dot{m}_h$ ($\dot{M}_{\rm Edd}$)	X_s (r_s)	R	Γ	χ^2/DOF
02345	0-60	$0.787^{+0.047}_{-0.044}$	$0.082^{+0.005}_{-0.004}$	$33.754^{+0.096}_{-0.048}$	$1.457^{+0.002}_{-0.001}$	$2.602^{+0.044}_{-0.044}$	74.59/79
	60-160	$0.772^{+0.027}_{-0.028}$	$0.074^{+0.003}_{-0.003}$	$38.884^{+0.314}_{-0.117}$	$1.496^{+0.002}_{-0.001}$	$2.546^{+0.038}_{-0.038}$	79.09/79
	160-260	$0.779^{+0.054}_{-0.053}$	$0.077^{+0.001}_{-0.004}$	$33.903^{+0.140}_{-0.058}$	$1.487^{+0.001}_{-0.001}$	$2.605^{+0.037}_{-0.037}$	57.49/79
	260-360	$0.793^{+0.039}_{-0.038}$	$0.108^{+0.002}_{-0.002}$	$24.151^{+0.065}_{-0.064}$	$1.372^{+0.001}_{-0.002}$	$2.539^{+0.034}_{-0.034}$	58.32/79
	360-460	$0.839^{+0.058}_{-0.058}$	$0.107^{+0.002}_{-0.001}$	$16.939^{+0.048}_{-0.047}$	$1.503^{+0.001}_{-0.001}$	$3.014^{+0.033}_{-0.033}$	68.11/79
02346	400-500	$0.599^{+0.034}_{-0.033}$	$0.020^{+0.002}_{-0.001}$	$65.837^{+0.061}_{-0.062}$	$1.222^{+0.002}_{-0.002}$	$2.475^{+0.034}_{-0.038}$	95.71/79
	500-600	$0.658^{+0.043}_{-0.047}$	$0.020^{+0.001}_{-0.002}$	$61.390^{+0.070}_{-0.072}$	$1.231^{+0.002}_{-0.001}$	$2.542^{+0.055}_{-0.051}$	103.52/79
	600-700	$0.676^{+0.055}_{-0.054}$	$0.020^{+0.001}_{-0.001}$	$60.351^{+0.088}_{-0.084}$	$1.232^{+0.001}_{-0.001}$	$2.516^{+0.044}_{-0.047}$	103.97/79
	700-800	$0.750^{+0.067}_{-0.062}$	$0.021^{+0.001}_{-0.001}$	$58.378^{+0.076}_{-0.071}$	$1.264^{+0.001}_{-0.001}$	$2.652^{+0.057}_{-0.058}$	100.38/79
	800-900	$0.766^{+0.077}_{-0.075}$	$0.022^{+0.002}_{-0.001}$	$56.031^{+0.084}_{-0.081}$	$1.285^{+0.001}_{-0.001}$	$2.707^{+0.039}_{-0.041}$	75.30/79
	900-1000	$0.767^{+0.047}_{-0.045}$	$0.023^{+0.001}_{-0.001}$	$55.671^{+0.067}_{-0.061}$	$1.543^{+0.001}_{-0.001}$	$2.759^{+0.049}_{-0.045}$	82.72/79

Within the first 60 s, the disk accretion rate decreases from 0.79 $\dot{M}_{\rm Edd}$ to 0.77 $\dot{M}_{\rm Edd}$, and consequently, the shock location also recedes from 33.8 r_s to 38.9 r_s. For the next 400 s, the disk accretion rate steadily increases from 0.77 $\dot{M}_{\rm Edd}$ to 0.84 $\dot{M}_{\rm Edd}$. As expected, the shock location decreases from 38.9 r_s to 16.9 r_s within this time span. This corresponds to a speed of the shock of about 2200 m s^{-1}. This agrees with our finding of the rapid increase in accretion rate in the disk. This is possible only if the effect is local and the supply at the outer edge may not be affected. The details of the analysis are provided in Table 2. The TCAF model fit of the unfolded spectrum for 0–60 s of observation is given in Figure 4 (right). In Figure 6 we show the default 68-90-99% confidence contours of TCAF fit parameters $\dot{m}_d$ with $\dot{m}_h$ and $\dot{m}_d$ with X_s.

In the case of the second orbit, we performed the spectral fitting only in the U-shaped region where the photon count rate first decreases very rapidly and then increases slowly. The *diskbb+power-law* fit in a span of 500 s shows a monotonic increase in the power-law slope, indicating a plausible transition toward the softer state. The disk rate increases from 0.60 $\dot{M}_{\rm Edd}$ to 0.77 $\dot{M}_{\rm Edd}$, and consequently, the shock location decreases from 65.8 r_s to 55.7 r_s within this span. The corresponding shock velocity is ∼900 m s^{-1}. The details of the fit parameters are shown in Table 2.

4. Summary and Concluding Remarks

In this paper, we presented our analysis of the spectral and timing behavior of GRS 1915+105 using the TCAF paradigm. For this purpose, the θ class data of the source as obtained by the LAXPC instrument of AstroSat satellite were used. To the best of our knowledge, this is the first time that the θ class data of AstroSat are analyzed with the TCAF paradigm. In this paradigm, different spectral states as well as the QPOs resulting

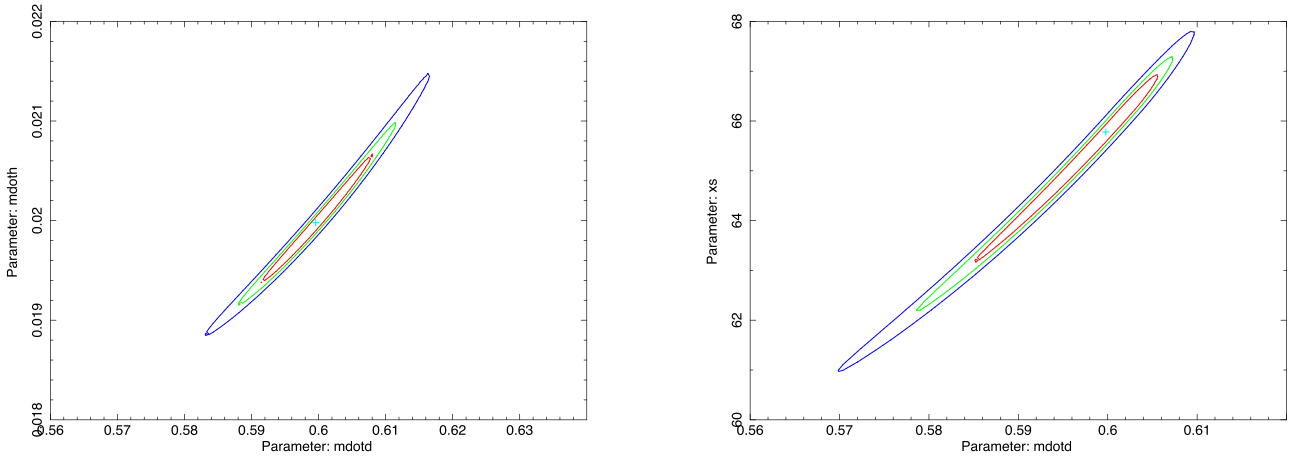

Figure 6. (Left) Default 68-90-99% confidence contours for TCAF fit parameters $\dot{m}_d$ and $\dot{m}_h$ are shown for the 400–500 s of observation in orbit 02346. (Right) Confidence contours for the same observation shown for $\dot{m}_d$ and X_s.

from resonance oscillation of the Compton cloud arise out of the interplay between two types of accretion rates, namely, the Keplerian disk rate ($\dot{m}_d$) and the sub-Keplerian halo rate ($\dot{m}_h$). In the sub-Keplerian flow, shocks are formed when the Rankine–Hugoniot conditions are satisfied (Chakrabarti 1989, 1996; Chakrabarti & Das 2004). If the Keplerian disk rate increases, it increases the soft-seed photons, and the post-shock region (CENBOL, which acts as a "Compton cloud") is cooled down rapidly, causing the shock to proceed toward the black hole. This has indeed been obtained in our spectral analysis. In the process, both the compressional heating timescale and the cooling timescale of the CENBOL decrease and become comparable (Chakrabarti et al. 2015), triggering shock oscillations that manifest as QPOs in the light curve. We first obtained the state of the system by estimating the photon index using the *phabs*(diskbb+power-law)* model. Throughout our analysis, the photon index (Γ) was found to be above 2.4, indicating that the source was either in the soft-intermediate state (SIMS) or in the soft state (SS). In the case of both orbits, Γ monotonically increases with the increase in photon flux, implying the transition from SS to SIMS. In the first orbit, Γ made an excursion from 2.5 to 3.0 during the 400 s span of spectral analysis, indicating the transition of the source from SIMS to SS. The gradual enhancement of the disk accretion rate and the consequent decline of the shock location were also obtained from the TCAF model fitting. The shock location moves from $39r_s$ to $17r_s$, while the disk accretion rate increases from 0.77 to 0.84 $\dot{M}_{\rm Edd}$. A similar trend was followed in the second orbit as well (Table 2). In the two orbits (02345 and 02346) we have analyzed, within a span of 400–500 s, the total flux changes by a factor of 3–5. The corresponding shock velocity is ∼2200 and 900 m s^{-1}, respectively. This is significantly higher than the shock velocity obtained earlier in the case of transient sources, which lie within 10–20 m s^{-1} (Chakrabarti et al. 2008; Nandi et al. 2012; Debnath et al. 2013). This suggests the possibility that the local modulation of the accretion rate is due to feedback from the outflow (Chakrabarti & Manickam 2000; Chakrabarti & Nandi 2000). All these results indicate that GRS 1915+105 went through repeated microflares when it was in θ class.

As the shock location moves closer and becomes weaker, the QPO frequency increases because the frequency is inversely proportional to the infall timescale from the shock. This behavior is common in the rising phase of transient BHCs (see Debnath et al. 2013 and references therein). Therefore, as the source transits from SIMS to SS, the QPO frequency should increase. This has been corroborated by our timing analysis. As shown in Figure 2(a) and (b), the QPO frequency shifts toward a higher frequency domain with time. Within the first 225 s of observation, in which the QPO is relatively prominent, the QPO frequency moves from 4.22 to 4.51 Hz in the first orbit. In the case of the second orbit, the QPO frequency monotonically increases from 2.90 to 4.33 Hz within 400 s (Table 1). During this period, the shock location also decreases from 65.8 r_s to 55.7 r_s (Table 2). These findings further suggest that an interplay of two accretion rates is at the root of the manifestation of the spectral and timing behaviors. We have further observed the lower-frequency QPO at ∼2 Hz in the first orbit. The integrated fractional rms is ∼6%.

GRS 1915+105 and IGR 17091-3624 exhibit several classes that can be well differentiated by the Comptonizing efficiency (Pal & Chakrabarti 2015). As the variability class moves from the harder (HS, HIMS) to the softer (SIMS, SS) states, cooling increases as the soft photon number increases. This shrinks the CENBOL, resulting in inward movement of the shock to increase the frequency of the low-frequency QPOs. It has been shown earlier that in the case of the χ class of GRS 1915+105 where the X-ray flux is steady, the accretion flow could be explained in the light of the TCAF paradigm (Banerjee et al. 2020). In the present paper, we demonstrated that even inside a single variable class, there are considerable changes in the shock properties and accretion rates. Inferences about the flow from our analysis agree with the TCAF paradigm, which explains the spectral and timing properties of GRS 1915+105 as due to the interplay between the Keplerian and sub-Keplerian flows, the launching of outflows from the CENBOL region, and the effects of radiative transfer within the sonic sphere of the outflow (Nandi et al. 2000). The outflow rate depends upon the spectral state (Chakrabarti 1999) as the outflow is cooled via inverse Comptonization of the intercepted soft-seed photons from the disk. This causes part of the outflow from the sonic sphere to fall back upon the accreting flow and modulate the accretion rate locally. Used time-dependent Monte Carlo simulations to investigate the effects of Compton cooling, confirming the reduction of outflow rate with increased thermal flux. This accretion flow feedback could explain the rapid variation in accretion rates and consequent shock location in a few tens to a few hundred seconds, with a shock

velocity (∼ a few hundred meters per second) significantly higher as compared to usual transient sources during their outbursts (∼ a few tens of meters per second). Figure 5(a) and (b) suggests a gradual increase in Keplerian disk accretion with the gradual rise in spectral softness in the U-shaped domain. With the increase in disk rate, the shock location moves inward, causing the QPO frequency to increase. However, as the spectral states grow softer with increasing disk rate, the strength of QPOs gradually diminishes. The upward trend of the dominant power with the photon intensity in Figure 2(a) and (b) and an explicit downward trend in Figure 3(a) and (b) are in agreement with the aforementioned QPO behavior. This interconnected nature of spectral and timing properties manifested in Figures 2, 3, and 4 are indicative that both effects are of the same origin, as suggested in the TCAF paradigm. For the first time, we are able to see how the TCAF fit parameters such as the accretion rates and the shock location change during rapid intensity variations in the count rate of the θ class of GRS 1915+105.

Theoretical investigation of the behavior of magnetic flux tubes under the influence of various competing forces in the TCAF configuration was carried out by Nandi et al. (2001). It was observed that the collapse of the flux tubes under magnetic tension would be the dominant phenomena in hot plasma (temperature $\geqslant 10^{10}$ K), which would expel matter in the transverse direction. This evacuation of disk matter explains the origin of "baby jets". However, the mass estimated to be contained in the baby jets was found to be one order of magnitude lower than the earlier estimate (Mirabel et al. 1998), which implies that sub-Keplerian flow can contribute to these evacuations as well. This picture is aligned with the qualitative scenario of the ejection of a Comptonizing region presented by Vadawale et al. (2001, 2003) to explain the association of large radio flares and soft dips. The importance of disk-jet interaction and the nature of ejecta in determining the X-ray variability patterns was highlighted by Klein-Wolt et al. (2002) as well. In the present paper, we focus our attention on the U-shaped variability of longer duration (∼a few hundred seconds). We find QPOs during the hard-intermediate state (bottom part of the U-shaped light curve) and their gradual disappearance in the regions of softer states. This implies that the CENBOL is present in the hard-intermediate state, although it may gradually form and weaken inside one U-shaped part of the light curve. Our proposed collapse of the base of the outflow and the modulation of the accretion rate due to the return flow, which is a natural consequence of the TCAF paradigm, is one possible way to explain this observation. More extensive spectro-temporal analysis to test this hypothesis for various other classes with different intensity profiles will be presented in upcoming papers.

In principle, all these classes could be described by the TCAF paradigm (see Chakrabarti & Nandi 2000; Nandi et al. 2000). However, one must quantitatively analyze each of these classes to obtain the true reason for the class transitions. It is also important to distinguish between an outburst, where the accretion rates are enhanced near the outer edge of the disk, and the present system where mini-outbursts are seen with similar enhancements of rates on a very short timescale, leading to the conclusion that the effect is local and could be triggered by the return outflows. This work is in progress and will be reported elsewhere.

We thank the anonymous referee for their comments that have improved the quality of the manuscript. We acknowledge the strong support from Indian Space Research Organization (ISRO) for the successful realization and operation of AstroSat mission. The authors also acknowledge the AstroSat team for the distribution. The LaxpcSoft software is used for the analysis. A.B. and A.B. acknowledge the support fellowship of the S. N. Bose National Centre for Basic Sciences, Kolkata, India. D.C. and D.D. acknowledge partial support of the DST/GITA sponsored India-Taiwan collaborative project fund (GITA/DST/TWN/P-76/2017). S.K.C. and D.D. acknowledge partial support from the ISRO sponsored RESPOND project (ISRO/RES/2/418/17-18) fund. Research of D.D. and S.K.C. is supported in part by the Higher Education Department of the Government of West Bengal, India. T.K. and H.M.A. acknowledge the support of the Department of Atomic Energy, Government of India, under project No. 12-R&D-TFR-5.02-0200.

Facility: Astrosat.

ORCID iDs

Anuvab Banerjee https://orcid.org/0000-0001-7796-8907
Ayan Bhattacharjee https://orcid.org/0000-0002-2878-4025
Debjit Chatterjee https://orcid.org/0000-0001-6770-8351
Dipak Debnath https://orcid.org/0000-0003-1856-5504
Sandip Kumar Chakrabarti https://orcid.org/0000-0002-0193-1136
Tilak Katoch https://orcid.org/0000-0002-9418-4001
H. M. Antia https://orcid.org/0000-0001-7549-9684

References

Agrawal, P. C., Yadav, J. S., Antia, H. M., et al. 2017, JApA, 38, 30
Antia, H. M., Yadav, J. S., Agrawal, P. C., et al. 2017, ApJS, 231, 10
Banerjee, A., Bhattacharjee, A., Debnath, D., & Chakrabarti, S. K. 2020, RAA, 20, 208
Banerjee, I., Bhattacharjee, A., Banerjee, A., et al. 2021, RAA, in press (arXiv:1904.11644)
Belloni, T., Klein-Wolt, M., Meńdez, M., van der Klis, M., & van Paradijs, J. 2000, A&A, 355, 271
Bhattacharjee, A. 2018, Astrophysics and Space Science Proc., Vol. 53, Exploring the Universe: From Near Space to Extra-Galactic (Heidelberg: Springer), 93
Bhattacharjee, A., Banerjee, I., Banerjee, A., et al. 2017, MNRAS, 466, 1372
Bhattacharjee, A., & Chakrabarti, S. K. 2017, MNRAS, 472, 1361
Bhattacharjee, A., & Chakrabarti, S. K. 2019, ApJ, 873, 119
Bhattacharjee, A., & Chakrabarti, S. K. 2020, JKAS, (arXiv:2012.14502)
Bhattacharjee, A., & Chakrabarti, S. K. 2021, JKAS, (arXiv:2101.01488)
Castro-Tirado, A. J., Brandt, S., & Lund, S. 1992, IAUC, 5590, 2
Chakrabarti, S., & Titarchuk, L. G. 1995, ApJ, 455, 623
Chakrabarti, S. K. 1989, ApJ, 347, 365
Chakrabarti, S. K. 1995, in Seventeenth Texas Symp. on Relativistic Astrophysics and Cosmology, Vol. 759, ed. H. Böhringer, G. E. Morfil, & J. Trumper (New York: New York Academy of Sciences), 546
Chakrabarti, S. K. 1996, ApJ, 464, 664
Chakrabarti, S. K. 1997, ApJ, 484, 313
Chakrabarti, S. K. 1999, A&A, 351, 185
Chakrabarti, S. K., & Das, S. 2004, MNRAS, 349, 649
Chakrabarti, S. K., Debnath, D., Nandi, A., & Pal, P. S. 2008, A&A, 489, L41
Chakrabarti, S. K., & Manickam, S. G. 2000, ApJ, 531, 41
Chakrabarti, S. K., Mondal, S., & Debnath, D. 2015, MNRAS, 452, 3451
Chakrabarti, S. K., & Nandi, A. 2000, InJPh, 75, 1
Chatterjee, D., Debnath, D., Chakrabarti, S. K., et al. 2016, ApJ, 827, 88
Chatterjee, D., Debnath, D., Chakrabarti, S. K., & Jana, A. 2019, Ap&SS, 364, 14
Chatterjee, K., Debnath, D., Banerjee, A., et al. 2020b, RAA, (arXiv:2006.09077)
Chatterjee, K., Debnath, D., Chatterjee, D., Jana, A., & Chakrabarti, S. K. 2020a, MNRAS, 493, 2452

Debnath, D., Chakrabarti, S. K., & Mondal, S. 2014, MNRAS, 440, L121
Debnath, D., Chakrabarti, S. K., & Nandi, A. 2013, AdSpR, 52, 2143
Debnath, D., Chatterjee, D., Jana, A., Chakrabarti, S. K., & Chatterjee, K. 2020, RAA, 20, 175
Debnath, D., Jana, A., Chakrabarti, S. K., Chatterjee, D., & Mondal, S. 2017, ApJ, 850, 92
Debnath, D., Molla, A. A., Chakrabarti, S. K., & Mondal, S. 2015b, ApJ, 803, 59
Debnath, D., Mondal, S., & Chakrabarti, S. K. 2015a, MNRAS, 447, 1984
Garain, S. K., Ghosh, H., & Chakrabarti, S. K. 2014, ApJ, 758, 114
Giri, K., & Chakrabarti, S. K. 2013, MNRAS, 430, 2836
Ingram, A., Done, C., & Fragile, P. C. 2009, MNRAS, 397, L101
Ingram, A., & van der Klis, M. 2015, MNRAS, 446, 3516
Jana, A., Chakrabarti, S. K., & Debnath, D. 2017, ApJ, 850, 91
Jana, A., Debnath, D., Chakrabarti, S. K., et al. 2016, ApJ, 819, 107
Jana, A., Debnath, D., Chakrabarti, S. K., & Chatterjee, D. 2020a, RAA, 20, 28
Jana, A., Debnath, D., Chatterjee, D., et al. 2020b, ApJ, 897, 3
Klein-Wolt, M., Fender, R. P., Pooley, G. G., et al. 2002, MNRAS, 331, 745
Markwardt, C. B., Swank, J. H., & Taam, R. E. 1999, ApJ, 513, L37
McClintock, J. E., & Remillard, R. A. 2006, in Black Hole Binaries, Compact Stellar X-ray Sources, ed. W. Lewin & M. van der Klis (Cambridge: Cambridge Univ. Press)
Mikles, V. J., Eikenberry, S. S., & Rothstein, D. M. 2006, ApJ, 637, 978
Mirabel, I. F., Dhaman, V., Chaty, S., et al. 1998, A&A, 330, L9
Misra, R., Yadav, J. S., Verdhan Chauhan, J., et al. 2017, ApJ, 835, 195
Molla, A. A., Debnath, D., Chakrabarti, S. K., et al. 2016, MNRAS, 460, 3163
Molteni, D., Sponholz, H., & Chakrabarti, S. K. 1996, ApJ, 457, 805
Mondal, S., Chakrabarti, S. K., & Debnath, D. 2015, ApJ, 798, 57
Mondal, S., Chakrabarti, S. K., & Debnath, D. 2016, Ap&SS, 361, 309
Mondal, S., Debnath, D., & Chakrabarti, S. K. 2014, ApJ, 786, 4
Muno, M. P., Morgan, E. H., & Remillard, R. A. 1999, ApJ, 527, 321
Nandi, A., Chakrabarti, S. K., Vadawale, S. V., & Rao, A. R. 2001, A&A, 380, 245
Nandi, A., Debnath, D., Mandal, S., & Chakrabarti, S. K. 2012, A&A, 542, A56
Nandi, A., Manickam, S. G., & Chakrabarti, S. K. 2000, arXiv:astro-ph/0012523
Pahari, M., Antia, H. M., Yadav, J. S., et al. 2017, ApJ, 849, 16
Pahari, M., Yadav, J. S., Verdhan Chauhan, J., et al. 2018, ApJL, 853, L11
Pal, P. S., & Chakrabarti, S. K. 2015, AdSpR, 56, 1784
Rao, A. R., Naik, S., Vadawale, S. V., & Chakrabarti, S. K. 2000, A&A, 360, L25
Rodriguez, J., Durouchoux, Ph., Mirabel, I., et al. 2002, A&A, 386, 271
Rodriguez, J., Shaw, S. E., Hannikainen, D. C., et al. 2008, ApJ, 675, 1449
Shakura, N. I., & Sunyaev, R. A. 1973, A&A, 24, 337
Shang, J. R., Debnath, D., Chatterjee, D., Jana, A., Chakrabarti, S. K., et al. 2019, ApJ, 875, 4
Singh, K. P., Stewart, G. C., Westergaard, N. J., et al. 2017, JApA, 38, 29
Sunyaev, R. A., & Titarchuk, L. G. 1980, A&A, 86, 121
Tagger, M., & Pellat, R. 1999, A&A, 349, 1003
Tanaka, Y., & Lewin, W. 1995, in X-Ray Binaries, ed. W. Lewin, J. vanParadijs, & P. van den Heuvel (Cambridge: Cambridge Univ. Press), 126
Vadawale, S. V., Chattopadhyay, T., Rao, A. R., et al. 2015, A&A, 578, A73
Vadawale, S. V., Rao, A. R., Naik, S., et al. 2003, ApJ, 597, 1023
Vadawale, S. V., Rao, A. R., Nandi, A., & Chakrabarti, S. K. 2001, A&A, 370, L17
Yadav, J. S., Agrawal, P. C., Antia, H. M., et al. 2016a, Proc. SPIE, 9905, 99051D
Yadav, J. S., Mishra, R., Chauhan, J. V., et al. 2016b, ApJ, 833, 27